

## Supporting information:

### Probing the Conductance of the $\sigma$ -System of Bipyridine Using Destructive Interference

Anders Borges<sup>†</sup>, E-Dean Fung<sup>‡</sup>, Fay Ng<sup>#</sup>, Latha Venkataraman<sup>‡,##</sup>, and Gemma C. Solomon<sup>†\*</sup>

<sup>†</sup>Department of Chemistry and Nano-Science Center, University of Copenhagen, 2100 Copenhagen Ø, Denmark <sup>‡</sup>Department of Applied Physics and Applied Mathematics, Columbia University, New York, New York 10027

<sup>#</sup>Department of Chemistry, Columbia University, New York, New York 10027

#### Contents:

#### S1. Experimental Procedures

*S1.1 Chemical Procedures*

*S1.2 STM Break-Junction Experimental Procedures*

#### S2. Additional Data and Analysis Procedures

*S2.1 Analysis of the occurrence of high and low conducting molecular junctions:*

*S2.2 2D Histograms for extended molecules*

#### S3. Theoretical Details

*S3.1 Details about junction geometries*

*S3.2 Description of partitioning scheme*

*S3.3 Explanation for why destructive interference feature is split*

*S3.4 Additional transmission plots*

*S3.5 Shifting of the molecular levels*

*S3.6 Justification for claims about  $\sigma$ -transport being dominated by gateway states*

*S3.7 Partitioned transmission for extended molecules*

#### S4. References

## **S1. Experimental Procedures**

### ***S1.1 Chemical Procedures***

Compounds **1**, **2** and **3** were acquired commercially. Compound **4** was synthesized and characterized in accordance with literature procedure.<sup>1</sup>

### ***S1.2 STM Break-Junction Experimental Procedures***

We measure the conductance of single molecules bound to gold electrodes using a custom Scanning Tunneling Microscope (STM). We use a 0.25 mm diameter gold wire (99.998%, Alfa Aesar) STM tip and a gold-coated (99.999%, Alfa Aesar) mica substrate. A commercial single-axis piezoelectric positioner (Mad City Labs) is used to achieve sub-angstrom level control of the tip-substrate distance. The STM is controlled using custom software in IgorPro (Wavemetrics, Inc.) and operated under ambient conditions at room temperature. The gold substrate is cleaned using UV/Ozone for 15 minutes prior to use. For each measurement, 1000 traces were first collected prior to adding molecular solutions to ensure that the gold was clean. Solutions of the target molecules at ~1 mM concentration in 1,2,4-trichlorobenzene (Alfa Aesar, > 99% purity) were added to the substrate for molecular conductance measurements. The applied bias was 225 mV, and the substrate was displaced at a speed of ~20 nm/s for all measurements. The current and voltage data were acquired at 40 kHz. For each molecule, we collected 6,000-10000 traces to create 1D and 2D conductance histograms without data selection. The 1D histograms were created using logarithm bins (100 bins/decade) and the 2D histograms were created by first aligning all traces at a conductance of  $0.5 G_0$  and then overlaying all measured traces in a two-dimensional plot.

## S2. Additional Data and Analysis Procedures

### S2.1 Analysis of the occurrence of high and low conducting molecular junctions

We employ a step-detection algorithm similar to those described in previous work to analyze the occurrence of high and low conducting molecular junctions.<sup>2,3</sup> We first determine the range of conductances corresponding to high conducting and low conducting molecular junctions by finding the local minima in the 1D histograms, as shown in Figure S1(a). This method returns similar values for both linearly binned and logarithmically binned histograms. For each trace, the number of points which lie within each conductance range is counted. Traces containing at least 20 points within a certain conductance range are considered to have a plateau at that conductance range, corresponding to a molecular junction. Traces are then categorized as having either only high conductance plateaus, only low conductance plateaus, or having both high and low conductance plateaus. By making 2D conductance histograms of each category, we can qualitatively confirm the validity of this step detection algorithm, as depicted in Figure S1(b,c).

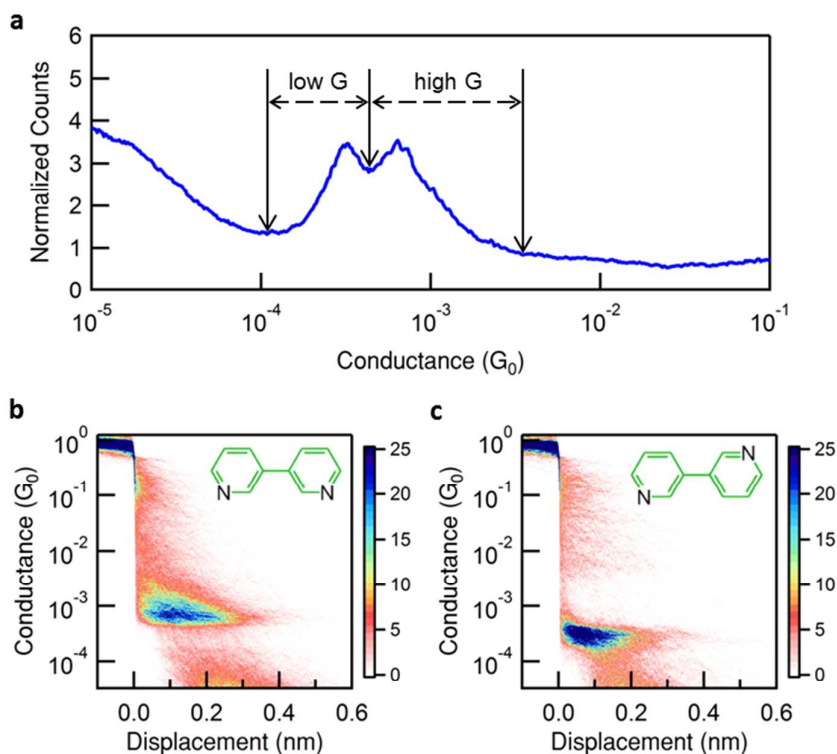


**Figure S1:** (a) 1D logarithmically binned histogram of **2** demonstrating how conductance ranges are determined. (b,c) 2D histograms of selected traces containing only high conducting junctions and only low conducting junctions, respectively.

Traces categorized as having both high and low conductance plateaus are further differentiated into those whose conductance goes from high to low from those whose conductance go from low to high. For each trace with two plateaus, we calculate the average position of points falling within each conductance range. If the points with high conductance occur on average earlier in the trace than the points with low conductance, we say that the trace goes from high to low conductance and vice versa.

The number of traces in each category is summarized in Table S1. Applying more stringent requirements for plateau detection predominantly affects how many high conducting traces also have a low conducting plateau. Because **2** does not form molecular junctions as readily as **1**, the number of traces showing no plateaus is also sensitive to the minimum points required to define a plateau. However, the number of traces that have only low conducting plateaus or that go from low to high conductance is robust to this parameter in the step-detection algorithm.

Molecule	minimum 20 points for plateau		minimum 100 points for plateau	
	1	2	1	2
Only High Plateau	589	1,369	2,942	2,586
Only Low Plateau	92	1,055	161	1,315
Both High and Low	9,281	5,892	6,775	2,791
High to Low	9,280	5,767	6,775	2,751
Low to High	1	125	0	40
No Plateaus Detected	38	1,684	122	3,308
Total Traces	10,000	10,000	10,000	10,000

**Table S1:** Summary of results from step-detection algorithm.

## S2.2 2D Histograms for extended molecules

Figure S2(a) and (b) show the 2D-histograms for molecules **3** and **4**, respectively. Figure S2(a) clearly shows two peaks, with the lower conducting peak occurring after the higher conducting peak just before breaking the junction, similar to **1**. The 2D histogram for **4** clearly does not show two conductance peaks.

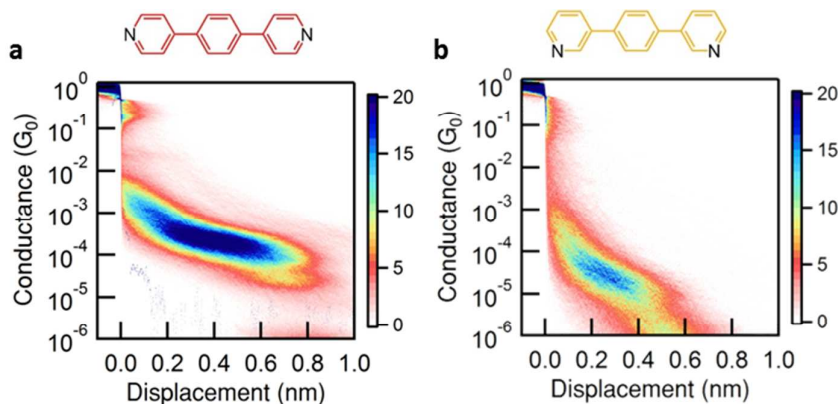


**Figure S2:** 2D histograms for (a) **3** and (b) **4**.

## S3. Theoretical Details:

### S3.1 Details about junction geometries

We used ASE/GPAW<sup>4-6</sup> to construct the junction geometries and calculate the transmissions. We used a hydrogen-like dzp basis<sup>7</sup> set for all elements along with the PBE functional. For the elements H, C and N the confinement energy used to generate the basis was 0.1 eV while for Au 0.01 eV was used. We constructed junction geometries consisting of four layers of Au atoms and modeled the tip with either a trimer or a four-atom pyramid on both sides of the Au layer. Periodic boundary conditions were employed to simulate a junction. The

innermost two layers of the Au slab was held fixed to the bulk position while the remaining atoms were relaxed to a maximum force lower than  $0.04 \text{ eV/\AA}$  for a variety of cell lengths to simulate different junction lengths. The resulting potential energy surfaces are shown in Figure S3. A grid spacing of  $0.20 \text{ \AA}$  was used along with a  $2 \times 2$  Monkhorst-Pack k-point sampling. We find that for the junction lengths with the lowest energy, the N-Au bond length varies between  $2.1$  and  $2.3$ . For the transport calculations we found that the  $\sigma$  transmission is very sensitive to the N-Au bond length. We therefore further relaxed the junctions using the finite difference mode to alleviate any basis set superposition error. Extra Au was added to the slab such that the slab consisted of 8 layers of Au fixed at the bulk positions along with a layer of relaxed Au on each surface and either a pyramid or trimer on top. From the Hamiltonian and overlap matrix of this latter geometry the transmission was calculated using a heavily modified version of the ASE transport calculator. A  $4 \times 4$  Monkhorst-Pack k-point grid was used to evaluate the conductance. To ensure there was no intercell coupling between molecules in neighboring cells we calculated the LUMO of the molecule in the junction for every k-point and found no variation in its values.

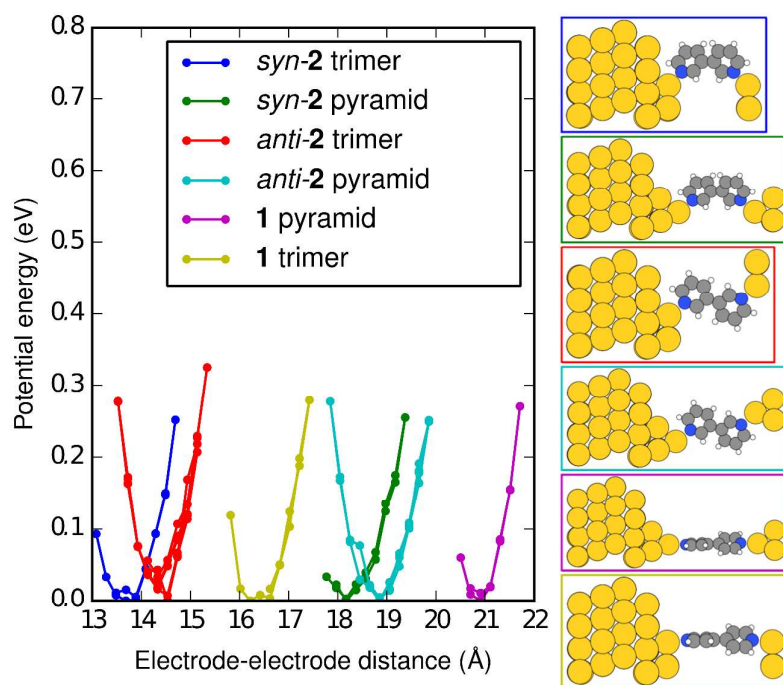


**Figure S3:** Potential energy surface of investigated junctions (left) and lowest energy structures used to calculate the transport(right). Colors relate potential energy surfaces, names and lowest energy structure used to calculate transport.

### S3.2 Description of partitioning scheme

Partitioning of the transmission in symmetry components require three steps: 1) Rotation of Hamiltonian and overlap matrix. 2) Obtaining self energies and

Green's function for molecule in the presence of Au. 3) Calculating partitioned transport. We go through each step in the following.

1) We rotated the basis set of the molecule in the junction to represent the local chemical environment of the individual atoms by block-diagonalizing the Hamiltonian of the junction corresponding to each atom. We then sorted the basis functions into those that were even and odd with respect to the plane of the ring. An example for **2** is seen in Figure S4. Figure S4(a) shows rotated basis functions for two neighboring atoms  $i$  and  $j$ . Those indicated with a purple box have even symmetry with respect to the ring, while those with odd symmetry are indicated with an orange box. Perfect partitioning of the basis set would imply that the overlap integrals between basis functions with different symmetry vanish. We therefore plot the overlap between the basis functions on neighboring atoms in Figure S4(b). As seen, the overlaps between basis functions assigned different symmetry are roughly zero, while those with the same symmetry have substantially larger overlap. Figure S4(c) illustrates the complete overlap matrix of the molecule and shows the same trend. This indicates reasonable partitioning of the basis set, as is also reflected by the partitioned transmission in the main paper.

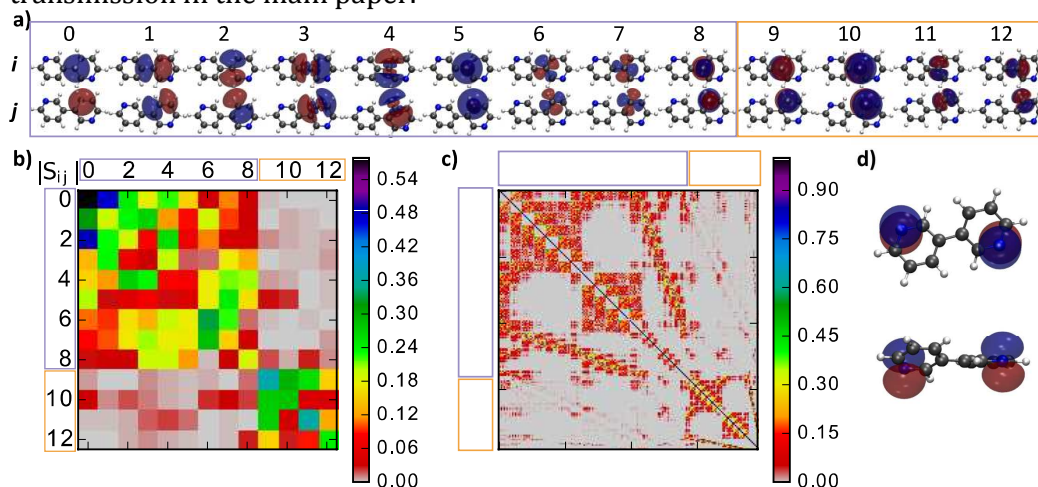


**Figure S4:** a) Sample basis functions rotated according to local chemical environment on two neighboring atoms. The purple box indicates those basis functions assigned  $\sigma$  symmetry, while the orange box indicates those basis functions assigned  $\pi$  symmetry. b) Overlap matrix between basis functions in a) Since  $i$  and  $j$  belong to different atoms the matrix is not symmetric. c) Overlap matrix of all basis functions in the molecule. Basis functions have been sorted according to symmetry. d) Basis functions used to evaluate  $\pi_0$  contribution to transport.

2) We obtained the self energy matrices from the junction Hamiltonian and overlap matrix in the rotated basis and a bulk calculation of Au. From the bulk calculation of Au we obtained the electronic coupling and overlap of principle layers (3 layers of Au). This allows us to calculate the Greens function of the first and last principle layer in the scattering region using the ASE transport calculator. Using the method of transition regions outlined by Thygesen and

Rubio<sup>8</sup> we then obtained the self energies and subsequently the Green's function of the molecule in the presence of the Au in the junction.

3)

We calculated the partitioned transmission labeled  $\pi_0$  as  $T(E) = \Gamma_{11}^L(E) |G_{1N}^r(E)|^2 \Gamma_{NN}^R(E)$ . Here  $\Gamma_{11/NN}^{L/R}$  is the  $1,1/N,N$ th element of the left/right broadening matrix as a result of coupling to Au. The basis functions labeled 1 and N are the p<sub>z</sub>-orbitals on the binding nitrogen atoms, which are shown in Figure S4(d) from two different angles. The full transmission was calculated as

$$T(E) = \sum_{i,j,k,l \in M} \Gamma_{ij}^L G_{jk}^r \Gamma_{kl}^R G_{li}^a$$

The sum runs over all basis functions of the molecule. Since all basis functions have been assigned either  $\sigma$  or  $\pi$  symmetry we can attribute all terms where  $i,j,k,l$  are  $\sigma(\pi)$  to "pure"  $\sigma(\pi)$  contributions to the transmission. The remaining terms capture "interference" between the  $\sigma$  and  $\pi$  systems.

### S3.3 Explanation for why destructive interference feature is split

Gorczak et al investigated the splitting of the destructive interference feature and explained it with through-space interactions and small distortions of the individual rings.<sup>9</sup> We explain the splitting of the destructive interference according to a set of rules first published by Markussen et al.<sup>10</sup> and later generalized to  $\pi$ -systems that include closed loops<sup>11</sup>. The rules lead to a series of diagrams from which the transmission can be evaluated. Far from resonances, the transmission is simply proportional to the absolute square of the sum of the diagrams.

A tight-binding model of **2** is shown in Figure S5, along with the possible diagrams where hopping terms are only included through chemical bonds. All onsite energies are set to zero. Notice that it is only possible to draw diagrams containing onsite loops on at least one carbon atom. Onsite loops contribute a factor  $E$  to the numerical value of the diagram. All diagrams contain an onsite loop, and accordingly  $E=0$  is a root of the sum of the diagrams. This leads to destructive interference in the  $\pi$ -system at  $E=0$ . Now consider allowing through-space contribution across the bond connecting the two rings. If second nearest neighbor coupling is allowed it is still impossible to draw a valid diagram that does not contain an onsite loop and destructive interference therefore still occurs at  $E=0$ . This is also exemplified in the figure. Allowing third nearest neighbor interactions, however, allows for drawing diagrams that do not contain onsite loops. All these diagrams have the same relative sign and therefore do not cancel. This means that  $E=0$  is not at root in the sum of the diagrams and destructive interference does not occur at  $E=0$ . It is these interactions that are responsible for splitting the destructive interference. To show this, we explicitly removed all coupling between elements in the DFT-Hamiltonian that are connected *ortho*- or *para*- to the leads and on opposite rings. We then calculated the transmission through this structure to get the transmission shown in figure S5(c). It is seen that the splitting of the interference feature is reduced by roughly 2 eV to less than 1 eV. The remaining splitting can be attributed to  $\pi$ -basis functions on the hydrogen atoms and the small difference in onsite

energies. We have also investigated the effect of scaling the third nearest neighbor interaction in model systems and found that the interference features remain in the band gap even after scaling with as much as a factor 4.0. This indicates that the destructive interference feature is robust despite being sensitive to small terms as has been shown previously<sup>12,13</sup>.

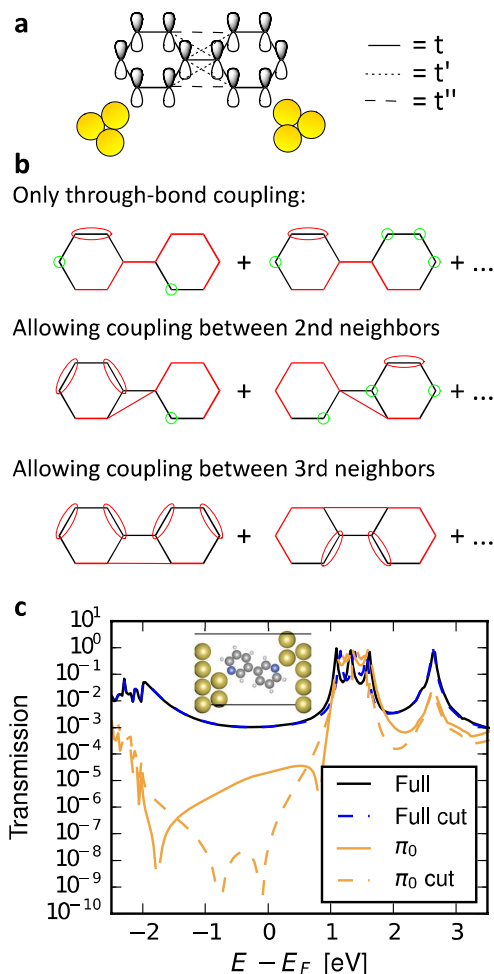


**Figure S5** a) Tight-binding model indicating considered interactions between sites on neighboring rings. b) Example diagrams that show that 3<sup>rd</sup> nearest neighbor interactions allow for diagrams without onsite loops. c) Transmission of a sample geometry of 2 before and after explicitly cutting coupling terms between 3<sup>rd</sup> nearest neighbors.

### S3.4 Additional transmission plots

We show in Figure S6 the calculated transmission plots for our lowest energy conformations shown in Figure S3. The energy levels of the molecules have not been shifted. The plot titles refer to the binding geometries.

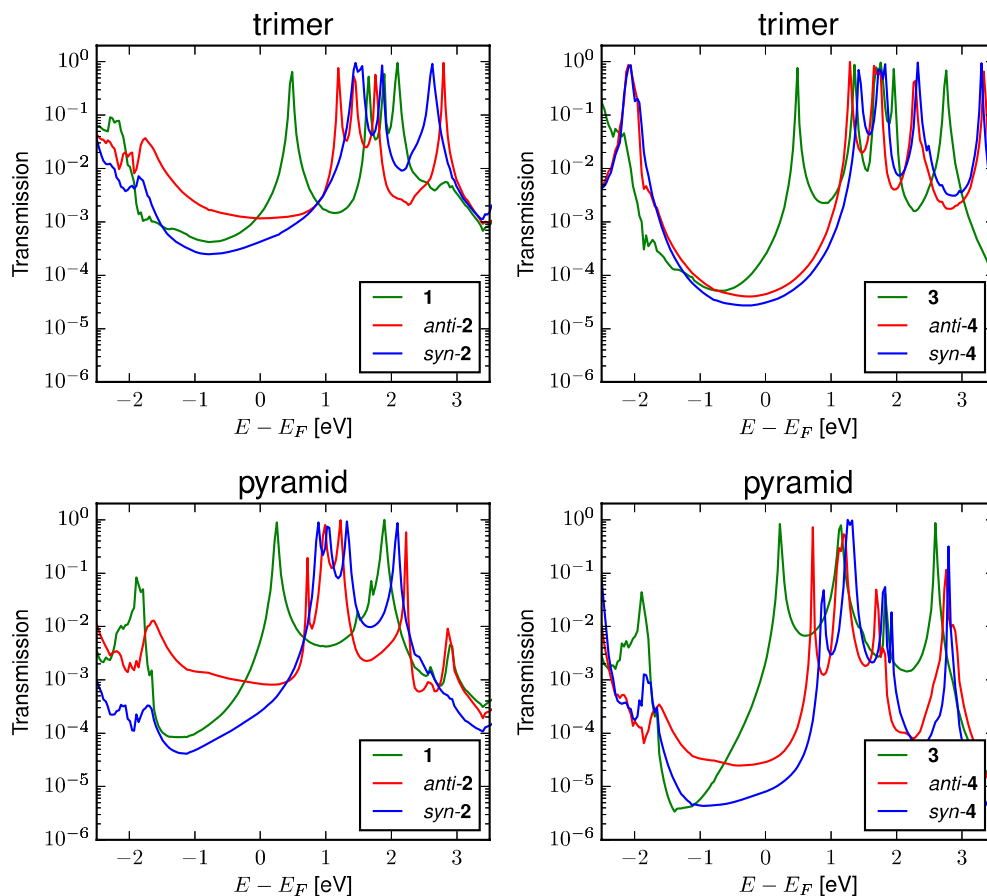


**Figure S6:** Calculated transmissions of the molecules with different binding geometries.

### S3.5 Shifting of the molecular levels

For the calculation of conductance in Figure 3(c), we corrected the band gap in accordance with the ionization potential (IP), electron affinity (EA) of the gas phase molecule and a screening potential based on an image charge model which has previously been used for **1**<sup>2</sup>. The Au was stripped from the junction geometry and a self-consistent calculation was run using the same settings as for the junction calculation. The shift of the occupied levels was determined as that which aligns the gas phase HOMO with the IP. The shift of the unoccupied levels was determined as that which aligns the gas phase LUMO with the EA. We used the experimentally determined IP of **1** reported as 9.10 eV. Table S2(S3) shows the energy of the HOMO(LUMO) calculated with Gaussian09d on the relaxed molecules using the 6-311G++(d,p) basis set and the unrelaxed molecules using GPAW with the same settings as for the junction calculation. It is seen that the energy levels of the **2** molecules are consistently shifted to slightly higher energy than **1**. We use the average shift of 0.38 eV as an estimate for the difference in IP of **1** and **2**. Similarly we use the average shift of 0.39 eV as an estimate for the relative EA of **1** and **2**. We use the EA of **1** reported to be 0.0293 at the EOM-CCSD(T)/aug-cc-pVDZ level of theory<sup>14</sup>.

<b>Funct.\Molecule</b>	<b>1</b>	<i>syn-2</i>	<i>anti-2</i>	<b>Max. diff.</b>
PBE	-6.17 (-5.80)	-5.98 (-5.57)	-6.07 (-5.67)	0.19 (0.23)
B3LYP	-7.42	-6.99	-6.98	0.44
CAM-B3LYP	-9.07	-8.37	-8.37	0,70
M06L	-6.44	-6.22	-6.26	0.22
<b>Average</b>	<b>-7.28</b>	<b>-6.89</b>	<b>-6.92</b>	<b>0.38</b>

**Table S2:** Energy of the HOMO of the gas phase molecules (in eV) for a variety of functionals. Numbers in parenthesis correspond to GPAW calculation of the molecule with the geometry in junction. All other structures are structures relaxed in the gas phase.

<b>Funct.\Molecule</b>	<b>1</b>	<i>syn-2</i>	<i>anti-2</i>	<b>Max. diff.</b>
PBE	-2.79 (-2.53)	-2.42 (-2.22)	-2.43 (-2.01)	0.37 (0.52)
B3LYP	-2.06	-1.67	-1.68	0.39
CAM-B3LYP	-0.80	-0.40	-0.40	0.40
M06L	-2.60	-2.20	-2.22	0.40
<b>Average</b>	<b>-2.06</b>	<b>-1.67</b>	<b>-1.68</b>	<b>0.39</b>

**Table S3:** Energy of the LUMO of the gas phase molecules for a variety of functionals. Numbers in parenthesis correspond to GPAW calculation of the molecule with the geometry in junction. All other structures are structures relaxed in the gas phase.

The rigid shift of energy levels as we have done here is valid in the limit of weak coupling to the leads and “smooth” density of states in the leads. Due to the strong hybridization of some of the molecular orbitals with the leads, the validity may be questioned. Furthermore, our calculation of the energy levels in the junction comes with a rather large uncertainty. For instance, it has been predicted that solvent can have large non-trivial effects on the energy levels of the molecule<sup>15,16</sup>. In light of this we investigated the robustness of our results in terms of energy shifts.

In Figure S7 we show the calculated conductance after shifting the occupied levels and taking the LUMO energy as a free variable as is done in the paper. We also show the conductance as function of the HOMO energy after shifting the LUMO energy. The conductance of both trimer and pyramid junctions decrease with increasing LUMO energy as expected. The conductance as function of HOMO also decreases with decreasing HOMO energy. After a certain threshold energy however, the conductance begins to increase. We have attributed the increase in conductance to unoccupied gateway states being shifted close to or even below the Fermi energy as a result of shifting the molecular energy levels. We note that this effect is important for shifts larger than the shifts predicted by our method (indicated by circles). Importantly, for realistic shifts of the frontier orbitals the calculations predict that **2** is a better conductor than **1**. The calculations are

therefore in good agreement with experimental observation that the conductance of **2** is higher than or similar to the conductance of **1**.

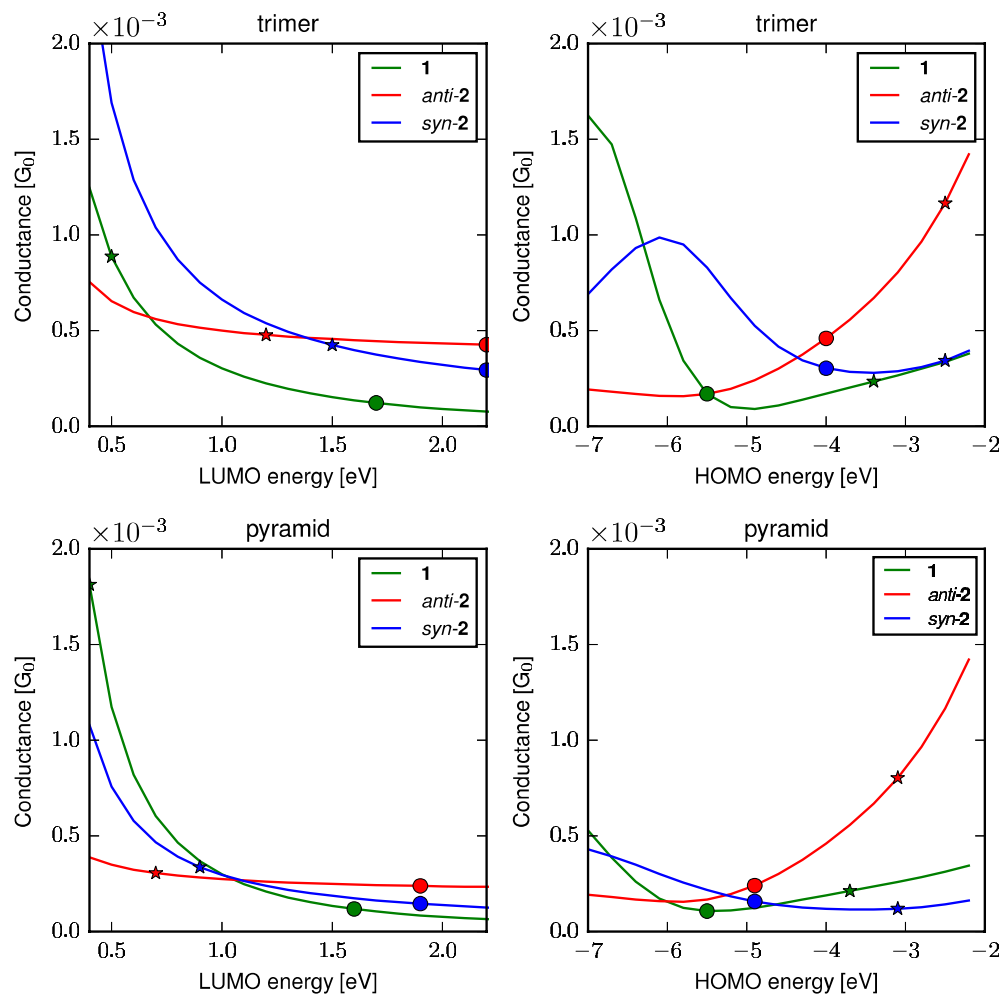


**Figure S7** Calculated conductance of **1** and **2** as function of frontier orbital energy for a fixed shift of occupied and unoccupied levels. Left column: Fixed shifts of occupied levels and varying unoccupied energy levels. Right column: Fixed shifts of unoccupied levels and varying occupied energy levels. Stars: Energy level predicted by DFT. Circles: Energy levels predicted by DFT+ $\Sigma$ .

We repeated the calculations for the extended molecules and the results are shown in Figure S8. It is seen that the calculated conductance of **3** is at least as high or higher than the conductance of **4** for realistic values of the frontier orbitals. This is in good agreement with the experiment.

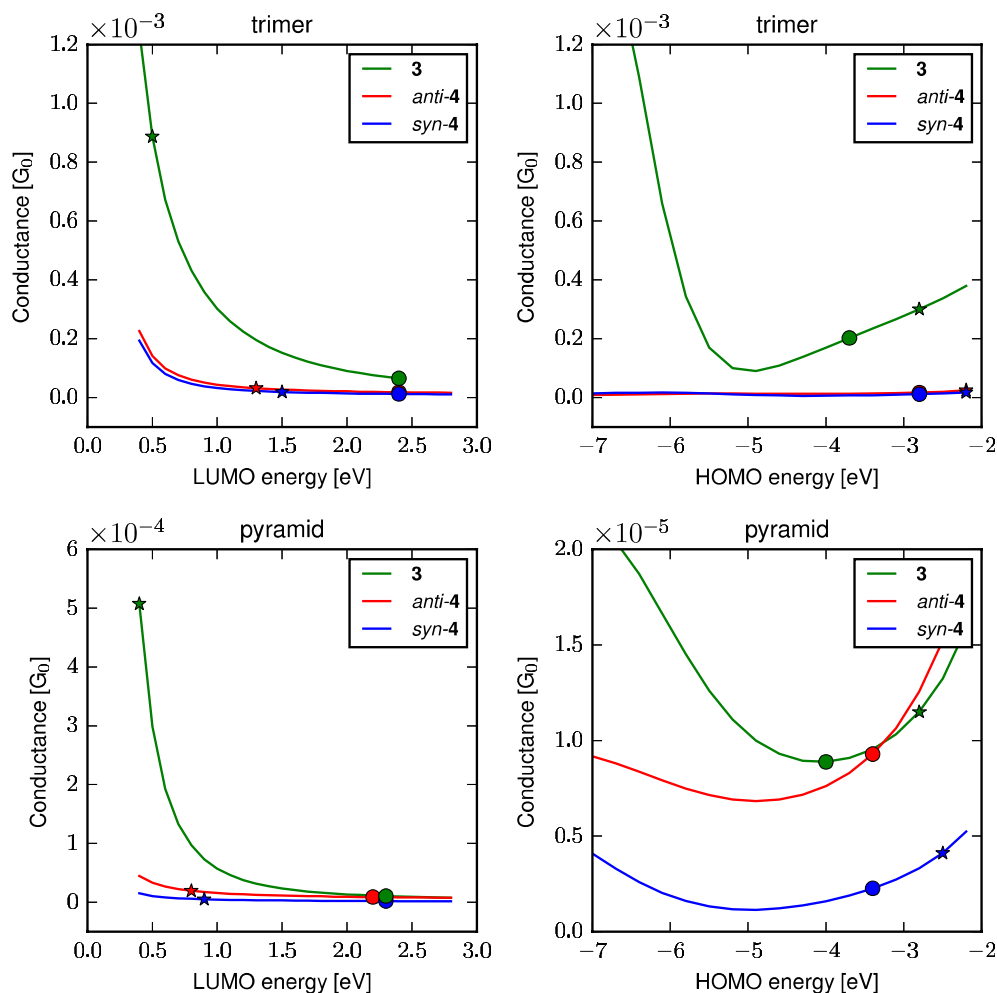


**Figure S8** Calculated conductance of **3** and **4** as function of frontier orbital energy for a fixed shift of occupied and unoccupied levels. Left column: Fixed shifts of occupied levels and varying unoccupied energy levels. Right column: Fixed shifts of unoccupied levels and varying occupied energy levels. Stars: Energy level predicted by DFT. Circles: Energy levels predicted by DFT+ $\Sigma$ .

### S3.6 Justification for claims about $\sigma$ -transport being dominated by gateway states

We first describe what we mean by gas phase orbitals and next calculate their contributions to the transport. The optimized geometries of the molecule in the junction resemble closely those optimized in the gas phase. We therefore took the geometry of the molecule in the junction, removed the Au atoms and ran a self-consistent  $\Gamma$ -point DFT calculation of the molecule to obtain the gas-phase molecular Hamiltonian. We then partitioned the basis set into  $\sigma$  and  $\pi$  as described in S3.2 and diagonalized the Hamiltonians spanned by each set. By diagonalizing these Hamiltonians, we get the gas phase molecular orbitals in the same basis as used in the junction. Since coupling between  $\sigma$  and  $\pi$  systems are relatively weak, the orbitals of  $\sigma$  and  $\pi$  systems look identical to the

eigenfunctions of the full gas phase molecular Hamiltonian. The orbitals come in pairs reflecting the even and odd combinations of the orbitals of each separate pyridine ring. We then perform a self-consistent  $\Gamma$ -point DFT calculation on the junction to obtain the junction Hamiltonian. The junction Hamiltonian is then expressed in the basis that diagonalizes the  $\sigma$  and  $\pi$  Hamiltonians in the gas phase. We can then partition the transmission into contributions from separate molecular orbitals as we did for the  $\sigma$  and  $\pi$  system. Figure S9 shows the contribution to transport through a variety of orbitals for *anti-2* without shifting the energy levels.

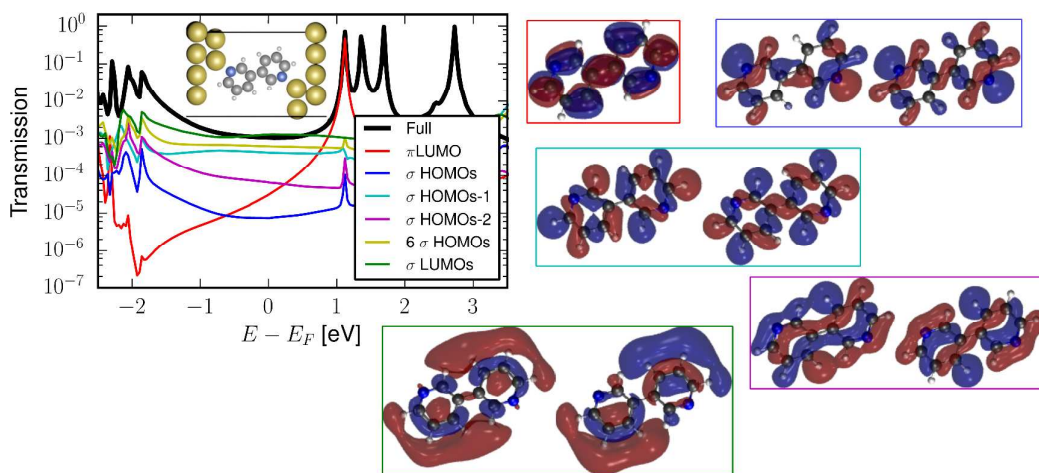


**Figure S9** Transmission partitioning in terms of gas phase orbitals before shifting of levels. Color of lines corresponds to orbitals with same box color.

We see that the highest contribution comes from the  $\sigma$  HOMOs-1 which constitutes 40 % of the transmission at the Fermi energy. Including the six highest occupied  $\sigma$  states reproduces 58% of the full transmission. Note that the LUMO does not contribute to transport. Since it requires several molecular orbitals to reproduce the full transmission, we argue that the  $\sigma$  contribution to transport cannot be understood in a simple way in terms of the molecular orbitals. Instead, gateway states are responsible for the transmission.

### S3.7 Partioned transmission for extended molecules

Finally, we can turn to transport calculations for molecules **3** and **4**, to illustrate that our atomistic calculations can also reproduce the trends observed in this case. Figure S10(a,b) shows the partitioned transmission of **3** and **4** at the  $\Gamma$ -point. We recognize that the  $\pi$  system of **3** completely dominates the transmission in the molecular bandgap with negligible contributions from the  $\sigma$  system. For **4** however, the contribution from the  $\pi$  system is negligible due to the destructive interference in the middle of the band gap. In spite of the close proximity of the pyridol-group to the electrodes, current injection through-space to the *para*-position of the *meta*-substituted systems does not mask the destructive interference feature completely. In contrast to **2**, the  $\sigma$  system no longer dominates transport in **4**. Instead, the figure shows that the dominating

contribution can be understood as a mixture of  $\sigma$  and  $\pi$ . The large magnitude of this contribution implies that the destructive interference in the  $\pi$  system can be masked by coupling to the  $\sigma$  system due to the torsional angle between neighboring rings. As a result, the calculated conductance of **4** is high enough to fall above the noise level in the experiment but below that of **3** as shown in Figure S10(c). This is in good agreement with the experiment: When the systems are extended to **3** and **4**, the increased length reduces the  $\sigma$  transport to such an extent that we recover the trend we expect from our understanding of the  $\pi$ -system from a simple Hückel model.

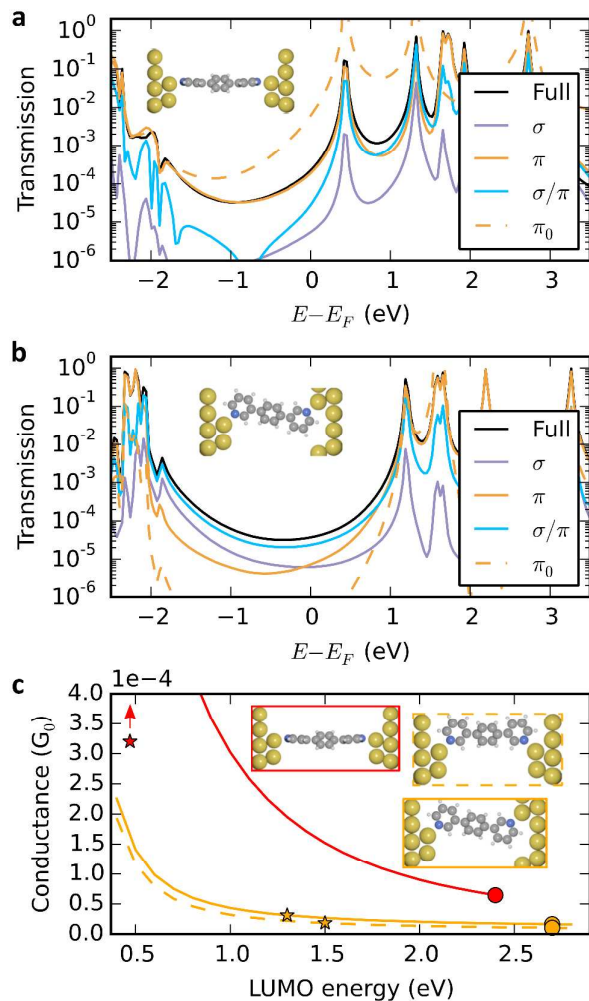


**Figure 10.** (a,b) Transmissions at the  $\Gamma$ -point for **3** and **4**. Black line: full transmission. Purple (orange) lines: contribution from the  $\sigma(\pi)$ -system. Cyan line: mixed  $\sigma/\pi$ -contribution. Dashed orange lines: transmission calculated assuming only the  $p_z$ -orbitals of the nitrogens couple to the leads (see supporting information for details). (c) Calculated conductance through three sample junctions as function of the energy of the LUMO. Stars indicate the energy captured by DFT. Circles indicate the predicted energy after shifting.

#### S4. References

- (1) Chaumeil, H.; Drian, C. Le; Defoin, A. *Synthesis (Stuttg)*. **2002**, 2002 (6), 757.
- (2) Quek, S. Y.; Kamenetska, M.; Steigerwald, M. L.; Choi, H. J.; Louie, S. G.; Hybertsen, M. S.; Neaton, J. B.; Venkataraman, L. *Nat. Nanotechnol.* **2009**, 4 (4), 230.
- (3) Aradhya, S. V.; Frei, M.; Hybertsen, M. S.; Venkataraman, L. *Nat. Mater.* **2012**, 11 (10), 872.
- (4) Bahn, S. R.; Jacobsen, K. W. *Comput. Sci. Eng.* **2002**, 4 (3), 56.
- (5) Mortensen, J. J.; Hansen, L. B.; Jacobsen, K. W. *Phys. Rev. B - Condens. Matter Mater. Phys.* **2005**, 71 (3), 35109.
- (6) Enkovaara, J.; Rostgaard, C.; Mortensen, J. J.; Chen, J.; Dułak, M.; Ferrighi, L.; Gavnholt, J.; Glinzvad, C.; Haikola, V.; Hansen, H. a; Kristoffersen, H. H.; Kuisma, M.; Larsen, a H.; Lehtovaara, L.; Ljungberg, M.; Lopez-Acevedo, O.; Moses, P. G.; Ojanen, J.; Olsen, T.; Petzold, V.; Romero, N. a; Stausholm-Møller, J.; Strange, M.; Tritsarlis, G. a; Vanin, M.; Walter, M.; Hammer, B.; Häkkinen, H.; Madsen, G. K. H.; Nieminen, R. M.; Nørskov, J. K.; Puska, M.; Rantala, T. T.; Schiøtz, J.; Thygesen, K. S.; Jacobsen, K. W. *J. Phys. Condens. Matter* **2010**, 22 (25), 253202.
- (7) Larsen, A. H.; Vanin, M.; Mortensen, J. J.; Thygesen, K. S.; Jacobsen, K. W. *Phys. Rev. B - Condens. Matter Mater. Phys.* **2009**, 80 (19), 1.
- (8) Thygesen, K.; Rubio, A. *Phys. Rev. B* **2008**, 77 (11), 115333.
- (9) Gorczak, N.; Renaud, N.; Tarkuç, S.; Houtepen, A. J.; Eelkema, R.; Siebbeles, L. D. A.; Grozema, F. C. *Chem. Sci.* **2015**, 6 (7), 4196.
- (10) Markussen, T.; Stadler, R.; Thygesen, K. S. *Nano Lett.* **2010**, 10 (10), 4260.
- (11) Pedersen, K. G. L.; Borges, A.; Hedegård, P.; Solomon, G. C.; Strange, M. J. *Phys. Chem. C* **2015**, 119 (48), 26919.
- (12) Solomon, G. C.; Bergfield, J. P.; Stafford, C. A.; Ratner, M. A. *Beilstein J. Nanotechnol.* **2011**, 2 (1), 862.
- (13) Pedersen, K. G. L.; Strange, M.; Leijnse, M.; Hedegård, P.; Solomon, G. C.; Paaske, J. *Phys. Rev. B* **2014**, 90 (12), 125413.
- (14) Bâldea, I. *Faraday Discuss.* **2014**, 174 (37), 1.
- (15) Bâldea, I. *Nanoscale* **2013**, 5 (19), 9222.
- (16) Bâldea, I.; Köppel, H.; Wenzel, W. *Phys. Chem. Chem. Phys.* **2013**, 15 (6), 1918.